



Radiation-assisted chemical short-range order formation in high-entropy alloys

Zhengxiong Su^a, Tan Shi^a, Huahai Shen^b, Li Jiang^c, Lu Wu^d, Miao Song^e, Zhiming Li^{f,*}, Sheng Wang^{a,*}, Chenyang Lu^{a,*}

^a Department of Nuclear Science and Technology, Xi'an Jiaotong University, Xi'an, 710049, China

^b Institute of Nuclear Physics and Chemistry, China Academy of Engineering Physics, Mianyang, 621900, China

^c School of Materials Science and Engineering, Dalian University of Technology, Dalian, 116024, China

^d The First Sub-institute, Nuclear Power Institute of China, Chengdu, 610041, China

^e Department of Nuclear Engineering and Radiological Sciences, University of Michigan, Ann Arbor, MI 48109, United States

^f School of Materials Science and Engineering, Central South University, Changsha, 410083, China

ARTICLE INFO

Article history:

Received 15 November 2021

Revised 29 December 2021

Accepted 17 January 2022

Keywords:

Chemical short-range order

High-entropy alloy

Radiation-enhanced diffusion

Transmission electron microscopy

ABSTRACT

The chemical short-range order (CSRO) in a face-centered cubic equiatomic NiCoFeCrMn high-entropy alloy was revealed directly from advanced transmission electron microscopy in this work. Further, instead of controlling CSRO by conventional heat treatment, we show a new possibility of tailoring CSRO by radiation. The multiple types of atoms in such high-entropy system are more prone to form CSRO under radiation compared to that only under thermodynamic equilibrium conditions, due to the rearrangement of the chemical ordering during the non-equilibrium thermal spike period and the radiation-enhanced diffusion mechanism. Our results show an increase in the fraction of CSRO area by ~45% after high-temperature irradiation with a dose of 50 DPA. Accordingly, we demonstrated that enhanced CSRO can be achieved by controlling the irradiation dose and temperature, which provides a new route to explore the kinetic evolution and effect of CSRO in complex alloy systems.

© 2022 Acta Materialia Inc. Published by Elsevier Ltd. All rights reserved.

High-entropy alloys (HEAs) are solid solution alloys that consist of multiple principal elements without distinction between solute and solvent, and are also called multi-principal element alloys [1,2]. As they are located in the middle region of the phase diagram, a large number of previously untouched complex concentrated alloys are developed, thus opening up a new field and attracting considerable attention [3,4]. The variety and uniqueness of different element combinations give it a significant advantage over conventional alloys in mechanical performance, oxidation resistance, corrosion resistance, and irradiation resistance [5–11]. In recent years, it has been realized that due to the complex chemical interactions among constituent species, HEAs are not random solid solutions and can form chemical short-range order (CSRO) structure [12–14]. CSRO refers to a configuration where different types of atoms have their own preference of ordering at a spatial scale in the first and next couple of nearest-neighbors, resulting in an atomic arrangement that deviates from an ideal random solid solution [15]. CSRO has a critical effect on the mechanical behavior

of HEAs, such as stacking fault energy and dislocation slip [16–19]. Thus, this feature is considered as one of the underlying roots of its significant distinction from conventional solid solution alloys.

It has been a challenge for researchers to characterize the CSRO directly by experiments for a long time. In fact, some previous experiments had to rely on indirect methods, such as fitting of data from X-ray diffraction or neutron diffraction, and it often required extensive calculations to demonstrate the existence of CSRO [20–23]. Recently, direct quantitative observation and analysis of CSRO became possible by aberration-corrected scanning transmission electron microscopy (STEM) [12,24]. In the face-centered cubic (FCC) NiCoV medium-entropy alloy, additional diffuse reflections information of the CSRO can be obtained at $\frac{1}{2}\{311\}$ positions by performing atomic imaging under the [112] zone axis instead of the conventional [110] zone axis. We note the difference that some previous studies identified intermetallic crystals or precipitates as CSRO [25–27], which is not the same as the sub-nanometer scale of CSRO in the single-phase solid solution alloy that we focus on in this study.

Based on the state-of-the-art method, it becomes practical to study the evolution kinetics of CSRO, which will provide another level of insight into the understanding of the unusual proper-

* Corresponding authors.

E-mail addresses: lizhiming@csu.edu.cn (Z. Li), shengwang@mail.xjtu.edu.cn (S. Wang), chenylu@xjtu.edu.cn (C. Lu).

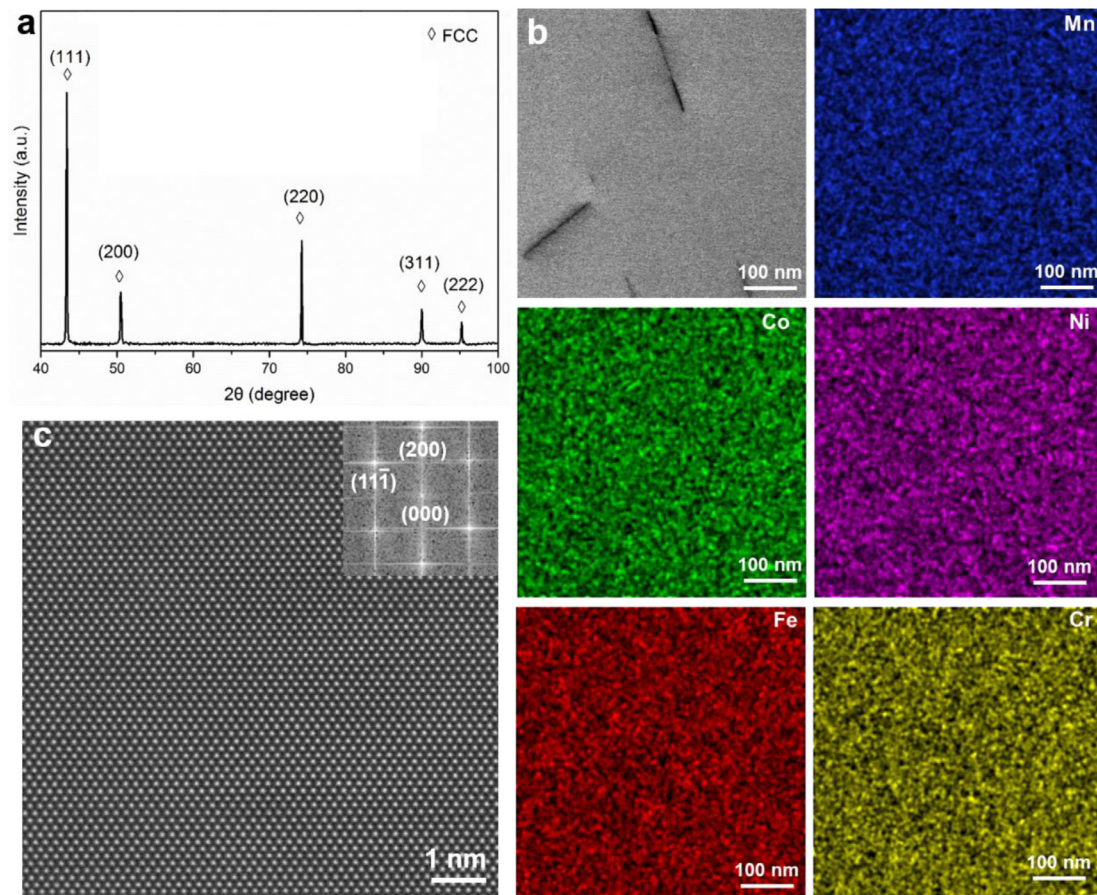


Fig. 1. Microstructure of NiCoFeCrMn alloys. (a) XRD pattern of NiCoFeCrMn; (b) STEM-EDS mapping for NiCoFeCrMn; (c) STEM-HAADF atomic image for NiCoFeCrMn with [110] zone axis, and the inset shows the corresponding FFT.

ties of HEAs. It is currently suggested that the fraction of CSRO can be regulated by different heat treatment methods [13,24]. For heat treatment, the structural reordering is driven by the conventional thermodynamic conditions controlled by time and temperature. High-temperature irradiation can be considered as an extreme thermodynamic process, where the radiation-induced displacement cascade can produce extremely high transient temperatures (several thousand Kelvin) and high-pressure shock waves (above 15 GPa) at a local spatial and time scale [28,29]. In addition, at a longer time scale, radiation-enhanced diffusion can further promote the rearrangement of atoms in a direction that favors structural energy stability. This is expected to be fundamentally different from and perhaps more effective than obtaining different degrees of CSRO through traditional thermodynamic processes (high-temperature annealing and homogenization). Moreover, to the best of our knowledge, the characterization of CSRO is still lacking in the most typical HEA of NiCoFeCrMn. It remains to be explored whether it has the same CSRO properties as the medium-entropy alloy. In this work, with the direct STEM observation, we studied the evolution of CSRO in single-phase equiatomic NiCoFeCrMn under 3 MeV Ni^{2+} self-ion irradiation at different temperatures and irradiation doses.

The metal elements of Ni, Co, Fe, Cr and Mn (purity 99.9%) were carefully weighed according to the predetermined equiatomic composition, and the mixed raw materials were melted for six times by an arc melting furnace. The obtained ingot was hot-rolled at 900 °C for a reduction ratio of 50% and then homogenized at 1200 °C for 2 h under the Ar atmosphere. The samples were mechanically polished with SiC sandpaper before irradiation, followed by vibration

polishing to remove the surface stress layer. The microstructure and CSRO were characterized on aberration-corrected STEM (FEI Themis Z) operating at 300 kV with a resolution better than 60 pm under normal conditions. Fig. 1a shows the X-ray diffraction (XRD) pattern of NiCoFeCrMn, representing a single-phase FCC structure. In order to reveal the elemental distribution of the samples, STEM-energy dispersive X-ray spectroscopy (EDS) analysis was carried out, as shown in Fig. 1b. The results confirm that the five principal elements are uniformly distributed. Fig. 1c presents the high angle annular dark-field (HAADF) atomic image along with [110] zone axis, together with the fast Fourier transform (FFT) pattern (inset in Fig. 1c). It can be seen that there is no additional diffraction information on the FFT except for the sharp Bragg spots from the FCC structure. This result is consistent with previous studies and suggests that no CSRO is detectable along the [110] zone axis for FCC HEAs [24,30].

To investigate the effect of irradiation dose and temperature on the evolution of CSRO, the samples were irradiated with 3 MeV Ni^{2+} at a fluence of 5×10^{16} ions/cm² at 420 °C and 540 °C, respectively. The flux is about 2.8×10^{12} ions/cm²/s. Cross-sectional TEM samples were prepared on an FEI Scios 2 Dual Beam workstation using focused ion beam (FIB) lift-out techniques. A “flash polishing” technique was used for sample cleaning on the FIB samples to eliminate damage caused by Ga ions [31]. The benefit of using cross-sectional samples is that the effects of different irradiation doses on CSRO can be studied directly at different depths. Fig. 2a shows STEM Bright Field (BF) cross-sectional images of irradiation defects with [110] zone axis at 420 °C and 540 °C, respectively. As the irradiation temperature increases, the disloca-

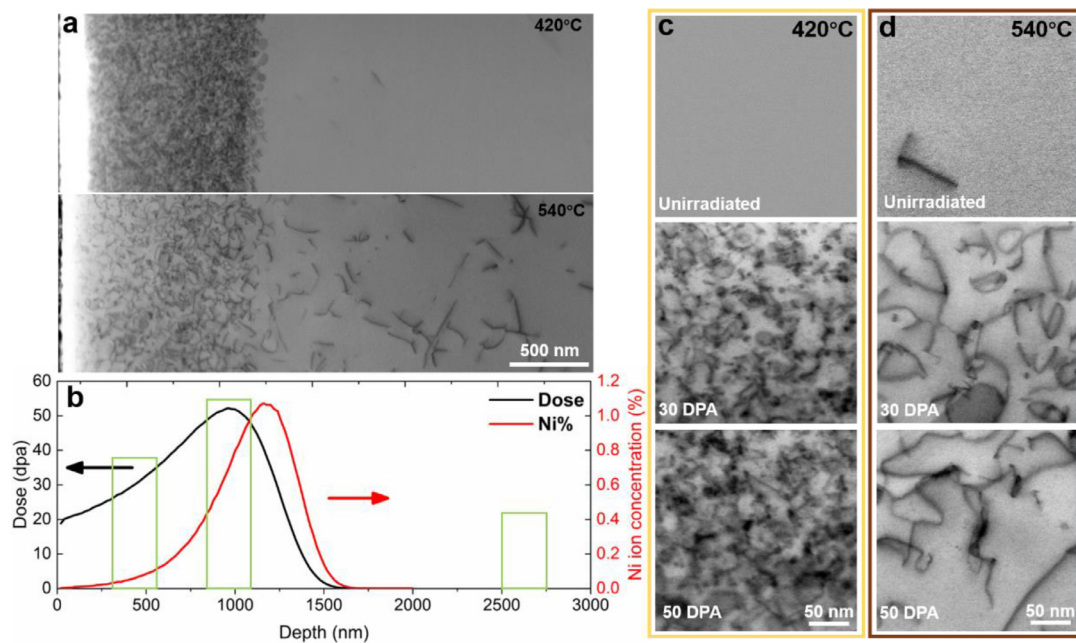


Fig. 2. (a) Cross-sectional on [110] zone STEM-BF images of NiCoFeCrMn irradiated with 3 MeV Ni²⁺ ions at a peak dose of 50 DPA at 420 °C and 540 °C, respectively. (b) The depth profiles of radiation dose and implanted Ni concentration were calculated using the SRIM-2013 software. (c) STEM-BF images of the defect microstructures in unirradiated region and regions of 30 DPA and 50 DPA at 420 °C and 540 °C, respectively.

tion loops migrate to a deeper depth. The variation of the displacement per atom (DPA) and the concentration of the injected Ni ions along the irradiation depth are shown in Fig. 2b. The calculation was determined using the quick Kinchin-Pease method in SRIM-2013 software, and the displacement threshold energy and binding energy for all elements were set to 40 eV and 0 eV, respectively [32]. The peak damage is about 50 DPA at a depth of 1000 nm. According to the SRIM calculation results, the irradiation depth does not exceed 1800 nm, but taking into account the high-temperature effect, we regard the region after 2600 nm as the unirradiated region. Therefore, based on the irradiation dose, three different regions were chosen at a depth of approximately 300 nm, 1000 nm and 2600 nm, corresponding to a dose of 30 DPA and 50 DPA and unirradiated region, respectively. These regions were further characterized by STEM, as shown in Fig. 2c. Furthermore, according to our experiments and previous reports, this irradiation condition does not lead to the formation of a second phase [33]. At 420 °C, the irradiation defects are mainly faulted loops of type $\langle 111 \rangle$, whereas the majority of dislocation loops transform to perfect loops of type $\langle 110 \rangle$ at 540 °C. As the irradiation temperature increases, the size of dislocation loops increases and the density decreases. This is mainly due to the enhancement of the interstitial diffusion by the high irradiation temperature, which promotes the merging and growth of dislocation loops based on loop transformation reactions. As a result, interstitial atoms at high temperatures (540 °C) migrate to deeper areas to form clusters.

Subsequently, we performed direct TEM observation of the CSRO distribution under different irradiation conditions. Fig. 3a-b are the HAADF atomic images along with [112] zone axis of the unirradiated region at 420 °C and 540 °C, respectively. It is clear from the FFT pattern (inset in Fig. 3a and b) that there is an additional diffuse disk (red circle) between the transmitted spot (000) and the $\{\bar{3}11\}$ diffraction spots. The hump (marked by arrow) in the diffraction intensity profile measured along the direction of the blue dashed line also confirms the presence of an additional disk (right panel). The HAADF images of the irradiated regions and the associated FFT patterns are also shown in Fig. S1. This result suggests the existence of additional ordered structures in addition to

the FCC phase. The size of each diffuse disk in reciprocal space is nearly one order of magnitude larger than that of Bragg spots. Therefore, it indicates that the corresponding coherency area in the actual space should be rather small, on a similar scale to the length of the CSRO.

As shown in Fig. 3c-e, using these extra diffuse disks based on the FFT information, we performed invert FFT (IFFT) transformation to obtain the distribution of CSRO (several marked by red circles) in the unirradiated, 30 DPA and 50 DPA regions at 420 °C. The regions with the presence of CSRO were lit up. The same values of contrast and brightness were used for all images. The size of CSRO and its corresponding area were measured and analyzed. We counted three IFFT images of each region to reduce statistical errors. The same method was applied to the sample irradiated at 540 °C. In addition, by performing IFFT transformations on the normal FCC $\{\bar{3}11\}$ spot and the diffuse disks between (000) spot and $\{\bar{3}11\}$ spots, respectively, the interplanar spacings of the CSRO is twice of the normal FCC lattice (as shown in Fig. S2). This explains why there are the extra diffuse disks at $\frac{1}{2}\{\bar{3}11\}$ positions in the FFT pattern. Furthermore, this relationship has also been confirmed by simulating diffraction pattern of CSRO configuration embedded in the FCC structure with the [112] zone axis [12,34]. The additional diffuse disks between (000) spot and $\{\bar{3}11\}$ spots are derived from CSRO, which is in accord with our results. The observations show that the CSRO exists in the NiCoFeCrMn HEA system, although the atomic sizes of these five elements (Ni, Co, Fe, Cr, Mn) are similar.

The distribution and average size of CSRO under different irradiation conditions are shown in Fig. 4a and b. In general, the majority (approximately 95%) of the CSRO sizes are smaller than 1 nm. The average size of the CSRO in the unirradiated region is about 0.60 nm for both 420 °C and 540 °C, which is similar to that of 0.65 nm in NiCoV medium-entropy alloy [12]. A slight reduction in the average CSRO size can be observed with increasing irradiation dose. The area fractions of CSRO in unirradiated, 30 DPA and 50 DPA region under 420 °C are 20%, 26% and 31%, respectively. When the irradiation temperature is increased to 540 °C, the area fractions in the corresponding regions increase to 24%, 29% and 33%, respectively. This indicates that the area fraction of CSRO is closely

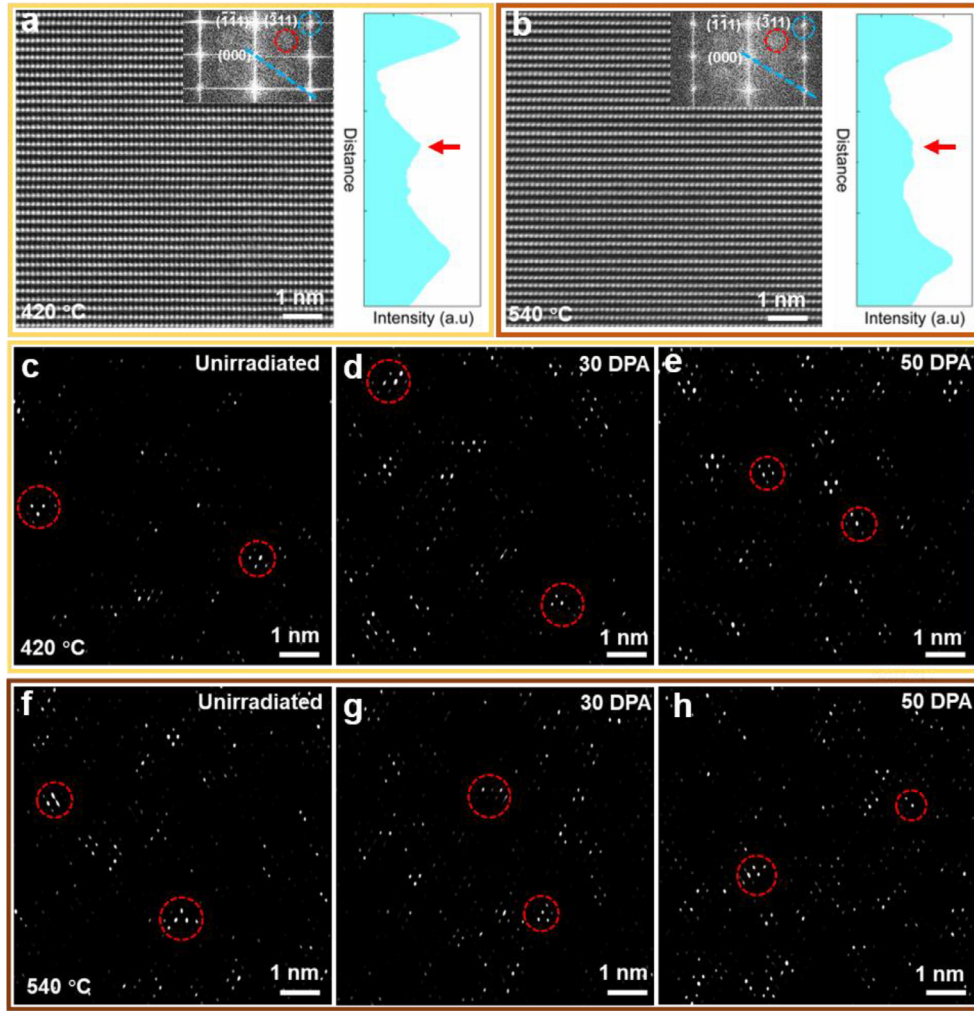


Fig. 3. (a)-(b) STEM-HAADF images of NiCoFeCrMn in the unirradiated region with the [112] zone axis at an irradiation temperature of 420 °C and 540 °C, respectively; the inset shows the corresponding FFT, where the red and blue dotted circles indicate diffuse disks at $\frac{1}{2}\{311\}$ positions and Bragg spots from FCC phase, respectively. Right panel: diffraction intensity along the blue dashed line. The red arrow indicates the intensity at $\frac{1}{2}\{311\}$ positions. (c)-(e) and (f)-(h) IFFT images of the CSRO in the region of unirradiated, 30 DPA and 50 DPA at 420 °C and 540 °C, respectively. Several CSRO regions are marked by red circles.

related to the irradiation dose and irradiation temperature, and increases moderately with the increase of dose and temperature.

Discussion

It should be recalled that a completely random solid solution is possible only at very high temperatures. However, in a real HEA system, there will inevitably be localized preferential (or avoided) bonding between certain near-neighbor species, along with strain relaxation to accommodate lattice distortions due to atomic size mismatch [19]. Previous work has shown inhomogeneities on the atomic level, where Fe and Co tend to be in Ni-poor regions rather than Cr and Mn using atomic-scale energy spectroscopy [35]. Recently, Zhang has obtained different degrees of CSRO in NiCoCr by annealing at different temperatures [13]. However, it can be seen that such strategy requires a long time (120 h) and a high temperature due to the constraint of self-interstitial atom diffusion under quasi-equilibrium thermodynamic conditions. It has been recognized that diffusion can be promoted by the movements of defects [36]. The irradiation of metals from high-energy particles produce two typical point defects: vacancy and interstitial atom [37,38]. As a significantly higher concentration of vacancies and interstitial atoms are produced by displacement cascades, radiation-enhanced diffusion (RED) will occur and lead to accelerated elemental diffu-

sion, especially at high temperature [39]. For instance, irradiation-induced segregation behavior at the dislocation loop is a direct consequence of RED (see Fig. S3). The RED coefficient is naturally much larger than the thermal diffusion coefficient due to the increase of point defect concentration [36]:

$$D_{\text{RED}} = D_v C_v + D_i C_i, \quad (1)$$

where D_{RED} represents the radiation-enhanced diffusion coefficient, D_v and D_i are the diffusion coefficients of vacancies and interstitials, and C_v and C_i are the concentrations of vacancies and interstitials, respectively. Rothman found that the self-diffusion rate of copper was increased by 10^6 times at 200 °C after irradiation as compared to that by thermal diffusion [40]. Thus, the diffusion coefficient can be increased by several orders of magnitude due to irradiation, which is more remarkable than that by heat treatment. Therefore, RED provides a strong driving force to regroup different types of atoms, which could be used to obtain an appreciable degree of CSRO in the HEAs. As seen in Fig. 4c, under the same thermodynamic conditions, the CSRO area fraction in the 50 DPA region is elevated by about 45% compared to that in the unirradiated region based on the results at 420 °C and 540 °C.

In addition, based on the chemical rate theory, in a steady-state system dominated by vacancy-interstitial recombination, the RED

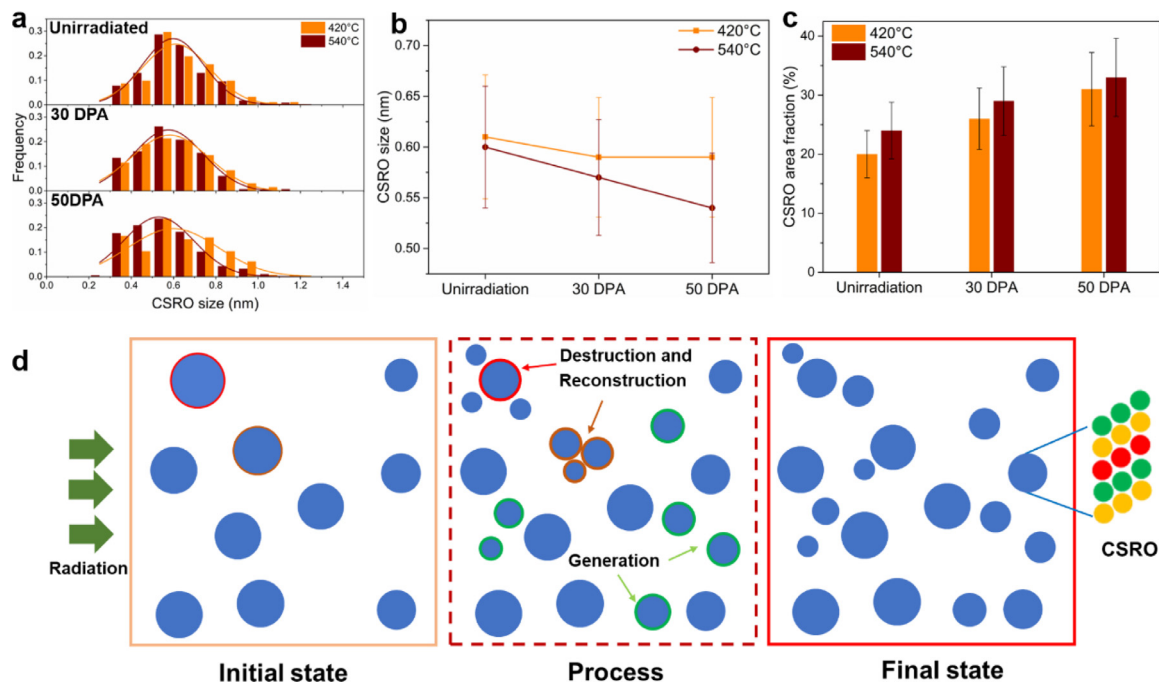


Fig. 4. (a) Size distribution, (b) average size and (c) area fraction of CSRO in the region of unirradiated, 30 DPA, and 50 DPA for an irradiation temperature of 420 °C and 540 °C, respectively. (d) Schematics of the CSRO kinetic process by radiation-enhanced diffusion in HEAs.

coefficient can be approximated as [41]:

$$D_{\text{RED}} = AK^{\frac{1}{2}} \exp\left(-\frac{E_m}{2kT}\right), \quad (2)$$

where K is the production rate of Frenkel pair, E_m represents the migration enthalpy of the slower-moving point defect, A is a constant associated with the material property, and kT is the product of Boltzmann's constant and temperature. The higher Frenkel pair generation rate K , proportional to DPA, enhances the RED coefficient, which leads to a more violent exchange between the lattice atoms in the material. Therefore, as shown in Fig. 4c, the area fraction of CSRO increases with increasing irradiation dose, and the relatively higher irradiation temperature also promote this process. This result of radiation-assisted CSRO formation is consistent with previous finding using the extended x-ray absorption fine structure method [20], but from the methodology point of view, there is no interference of fitting parameters and correlation artifacts in our characterization technique, and higher radiation dose was applied so that the increase of CSRO is much more evident. It has been shown by lattice kinetic Monte Carlo model that diffusion rates are also related to element type and concentration in multicomponent alloys, and the chemical complexity contributes to chemically-biased and sluggish diffusion [42–44]. Further study of the impact of RED on SRO requires understanding of the complex diffusion behaviors of different atom species in HEA at longer time scale. In addition to the RED mechanism, within the extremely short period of thermal spike (around 10 ps), the cascade collisions from irradiation could directly lead to the rearrangement of atoms in the melted core region, which could also favor the formation of CSRO structure from a random solid solution [45]. Under the mutual action of cascade collision and thermal recovery, the radiation-assisted process is accompanied by the generation, destruction and reconstruction of CSRO, as shown in the schematic in Fig. 4d. As a result, the size of the CSRO is slightly reduced, and its distribution becomes broader, but in general its average size remains relatively stable. In addition, previous studies showed that the size of the CSRO obtained by deformation or different heat treatments also remains almost unchanged, and the elemental dis-

tribution is uniform on the nanoscale based on atom probe tomography [12,24]. This means that CSRO is not a nucleated embryo of precipitates or second phase but an intrinsic feature of HEAs [24]. It can be expected that the precise control of CSRO will be achieved with the appropriate dose and temperature of irradiation. The local chemical environment of multi-component alloys is varied and this compositional complexity affects all aspects of the microstructure evolution, such as lattice distortion, point defect diffusion, defect cluster nucleation, etc. [46–48]. The existence of CSRO further alters the preferred local atom configurations and varies local defect energy in the system. This undoubtedly affects the preferential diffusion and percolation of various elements, thus contributing to chemically-biased and sluggish diffusion [42–44]. Subsequently, such atomic transport behavior would act on the nucleation and recombination of defects, and influence the defect microstructure.

It needs to be noted that irradiation-induced CSRO expands our current understanding on the aspects of irradiation effects involved in HEAs. Previously, when we characterized and analyzed the irradiated material, we generally focused on the effect of larger defects, such as dislocation loops/voids. It is now realized that the atomic arrangement, i.e., CSRO of the material, can also be changed at sub-nanometer scale, which adds a previously neglected influence factor when studying the relationship between microscopic defects and macroscopic mechanical properties of irradiated materials. Thus, the change of matrix properties by radiation-induced CSRO needs to be considered when evaluating the radiation response of high entropy alloys.

In summary, our experimental results with FFT and IFFT atomic-resolution lattice images show that CSRO exists even for NiCoFe-CrMn with such similar atomic sizes and low mixing enthalpies. Furthermore, it is effective to increase the fraction of CSRO in HEAs by properly enhancing the irradiation dose and irradiation temperature. Thus, radiation-assisted CSRO formation has shown to be attractive in regulating the CSRO in HEAs. This work presents a new strategy for tuning the degree of CSRO by radiation, and also paves a new way for further probing the kinetics evolution and role of CSRO in HEAs.

Declaration of Competing Interest

The authors declare no conflict of interest.

Acknowledgements

This work is supported by the National Key Research and the Development Program of China under Grant No.2019YFA0209900; the National Natural Science Foundation of China under Grant No. 12075179 and No. 51971248; the China Postdoctoral Science Foundation under Grant No. 2021M702583. In addition, we thank Instrument Analysis Center of Xi'an Jiaotong University for TEM characterization.

Supplementary materials

Supplementary material associated with this article can be found, in the online version, at doi:[10.1016/j.scriptamat.2022.114547](https://doi.org/10.1016/j.scriptamat.2022.114547).

References

- [1] E.P. George, D. Raabe, R.O. Ritchie, *Nat. Rev. Mater.* (2019).
- [2] Y.F. Ye, Q. Wang, J. Lu, C.T. Liu, Y. Yang, *Mater. Today* 19 (6) (2016) 349–362.
- [3] D.B. Miracle, O.N. Senkov, *Acta Mater.* 122 (2017) 448–511.
- [4] Y. Zhang, T.T. Zuo, Z. Tang, M.C. Gao, K.A. Dahmen, P.K. Liaw, Z.P. Lu, *Prog. Mater. Sci.* 61 (2014) 1–93.
- [5] B. Gludovatz, A. Hohenwarter, K.V. Thurston, H. Bei, Z. Wu, E.P. George, R.O. Ritchie, *Nat. Commun.* 7 (2016) 10602.
- [6] T. Yang, Y. Zhao, Y. Tong, Z. Jiao, J. Wei, J. Cai, X. Han, D. Chen, A. Hu, J. Kai, *Science* 362 (6417) (2018) 933–937.
- [7] Z. Li, K.G. Pradeep, Y. Deng, D. Raabe, C.C. Tasan, *Nature* 534 (7606) (2016) 227–230.
- [8] H. Luo, S.S. Sohn, W. Lu, L. Li, X. Li, C.K. Soundararajan, W. Krieger, Z. Li, D. Raabe, *Nat. Commun.* 11 (1) (2020).
- [9] C. Lu, L. Niu, N. Chen, K. Jin, T. Yang, P. Xiu, Y. Zhang, F. Gao, H. Bei, S. Shi, *Nat. Commun.* 7 (2016) 13564.
- [10] J. Lu, H. Zhang, Y. Chen, L. Li, X. Liu, W. Xiao, N. Ni, X. Zhao, F. Guo, P. Xiao, *Corros. Sci.* 180 (2021).
- [11] T. Shi, P.-H. Lei, X. Yan, J. Li, Y.-D. Zhou, Y.-P. Wang, Z.-X. Su, Y.-K. Dou, X.-F. He, D. Yun, *Tungsten* (2021) 1–21.
- [12] X. Chen, Q. Wang, Z. Cheng, M. Zhu, H. Zhou, P. Jiang, L. Zhou, Q. Xue, F. Yuan, J. Zhu, X. Wu, E. Ma, *Nature* 592 (7856) (2021) 712–716.
- [13] R. Zhang, S. Zhao, J. Ding, Y. Chong, T. Jia, C. Ophus, M. Asta, R.O. Ritchie, A.M. Minor, *Nature* 581 (7808) (2020) 283–287.
- [14] E. Antillon, C. Woodward, S.I. Rao, B. Akdim, T.A. Parthasarathy, *Acta Mater.* (2020).
- [15] E. Ma, X. Wu, *Nat. Commun.* 10 (1) (2019).
- [16] J. Ding, Q. Yu, M. Asta, R.O. Ritchie, *Proc. Natl. Acad. Sci. U S A* 115 (36) (2018) 8919–8924.
- [17] S. Yin, Y. Zuo, A. Abu-Odeh, H. Zheng, X.G. Li, J. Ding, S.P. Ong, M. Asta, R.O. Ritchie, *Nat. Commun.* 12 (1) (2021) 4873.
- [18] Q.J. Li, H. Sheng, E. Ma, *Nat. Commun.* 10 (1) (2019) 3563.
- [19] E. Ma, *Scr. Mater.* 181 (2020) 127–133.
- [20] F.X. Zhang, S. Zhao, K. Jin, H. Xue, G. Velisa, H. Bei, R. Huang, J.Y.P. Ko, D.C. Pagan, J.C. Neufeld, W.J. Weber, Y. Zhang, *Phys. Rev. Lett.* 118 (20) (2017) 205501.
- [21] A. Fantin, G.O. Lepore, A.M. Manzoni, S. Kasatnikov, T. Scherb, T. Huthwelker, F. d'Acapito, G. Schumacher, *Acta Mater.* (2020).
- [22] L.R. Owen, H.Y. Playford, H.J. Stone, M.G. Tucker, *Acta Mater.* 115 (2016) 155–166.
- [23] Y. Ma, Q. Wang, C. Li, L.J. Santodonato, M. Feygenson, C. Dong, P.K. Liaw, *Scr. Mater.* 144 (2018) 64–68.
- [24] D. Liu, Q. Wang, J. Wang, X. Chen, P. Jiang, F. Yuan, Z. Cheng, E. Ma, X. Wu, *Mater. Today Nano* (2021).
- [25] Y. Wang, D. Jiang, W. Yu, S. Huang, D. Wu, Y. Xu, X. Yang, *Mater. Des.* 181 (2019) 107981.
- [26] J. Moon, S.I. Hong, J.B. Seol, J.W. Bae, J.M. Park, H.S. Kim, *Mater. Res. Lett.* 7 (12) (2019) 503–509.
- [27] P. Singh, A. Marshal, A.V. Smirnov, A. Sharma, G. Balasubramanian, K. Pradeep, D.D. Johnson, *Phys. Rev. Mater.* 3 (7) (2019) 075002.
- [28] L.K. Béland, Y.N. Osetsky, R.E. Stoller, *npj Comput. Mater.* 2 (1) (2016).
- [29] Q. Peng, F. Meng, Y. Yang, C. Lu, H. Deng, L. Wang, S. De, F. Gao, *Nat. Commun.* 9 (1) (2018) 4880.
- [30] J.B. Seol, J.W. Bae, J.G. Kim, H. Sung, Z. Li, H.H. Lee, S.H. Shim, J.H. Jang, W.-S. Ko, S.I. Hong, H.S. Kim, *Acta Mater.* 194 (2020) 366–377.
- [31] C. Lu, K. Jin, L.K. Beland, F. Zhang, T. Yang, L. Qiao, Y. Zhang, H. Bei, H.M. Christen, R.E. Stoller, L. Wang, *Sci. Rep.* 6 (2016) 19994.
- [32] R.E. Stoller, M.B. Toloczko, G.S. Was, A.G. Certain, S. Dwaraknath, F.A. Garner, *Nucl. Instrum. Methods Phys. Res. Sect. B* 310 (2013) 75–80.
- [33] T.-n. Yang, C. Lu, G. Velisa, K. Jin, P. Xiu, Y. Zhang, H. Bei, L. Wang, *Scr. Mater.* 158 (2019) 57–61.
- [34] L. Zhou, Q. Wang, J. Wang, X. Chen, P. Jiang, H. Zhou, F. Yuan, X. Wu, Z. Cheng, E. Ma, *Acta Mater.* (2021).
- [35] Q. Ding, Y. Zhang, X. Chen, X. Fu, D. Chen, S. Chen, L. Gu, F. Wei, H. Bei, Y. Gao, M. Wen, J. Li, Z. Zhang, T. Zhu, R.O. Ritchie, Q. Yu, *Nature* 574 (7777) (2019) 223–227.
- [36] G.S. Was, *Fundamentals of Radiation Materials Science: Metals and Alloys*, 2007.
- [37] K. Nordlund, S.J. Zinkle, A.E. Sand, F. Granberg, R.S. Averback, R.E. Stoller, T. Suzudo, L. Malerba, F. Banhart, W.J. Weber, F. Willaime, S.L. Dudarev, D. Simeone, *J. Nucl. Mater.* 512 (2018) 450–479.
- [38] X. Zhang, K. Hattar, Y. Chen, L. Shao, J. Li, C. Sun, K. Yu, N. Li, M.L. Taheri, H. Wang, J. Wang, M. Nastasi, *Prog. Mater. Sci.* 96 (2018) 217–321.
- [39] J. Bourgoin, J. Corbett, *Radiat. Eff.* 36 (3–4) (1978) 157–188.
- [40] S. Rothman, *Phase Transformations During Irradiation*, 1983.
- [41] Y.S. Lee, R. Averback, C. Flynn, *Philos. Mag. Lett.* 70 (5) (1994) 269–276.
- [42] Y. Osetsky, A.V. Barashev, L.K. Béland, Z. Yao, K. Ferasat, Y. Zhang, *npj Comput. Mater.* 6 (1) (2020).
- [43] K. Ferasat, Y.N. Osetsky, A.V. Barashev, Y. Zhang, Z. Yao, L.K. Béland, *J. Chem. Phys.* 153 (7) (2020) 074109.
- [44] Y. Osetsky, A.V. Barashev, Y. Zhang, *Curr. Opin. Solid State Mater. Sci.* 25 (6) (2021).
- [45] L. Koch, F. Granberg, T. Brink, D. Utt, K. Albe, F. Djurabekova, K. Nordlund, *J. Appl. Phys.* 122 (10) (2017).
- [46] Q.F. He, P.H. Tang, H.A. Chen, S. Lan, J.G. Wang, J.H. Luan, M. Du, Y. Liu, C.T. Liu, C.W. Pao, Y. Yang, *Acta Mater.* (2021).
- [47] F.-H. Cao, Y.-J. Wang, L.-H. Dai, *Acta Mater.* 194 (2020) 283–294.
- [48] B. Xing, X. Wang, W.J. Bowman, P. Cao, *Scr. Mater.* 210 (2022).